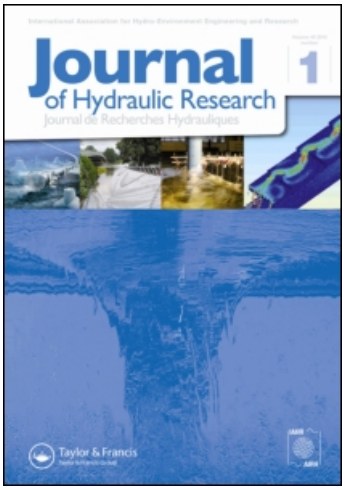

Journal of Hydraulic Research
Publication details, including instructions for authors and subscription information:
http://www.informaworld.com/smpp/title~content=t916282780

Mixing and re-entrainment in a negatively buoyant jet

Simone Ferrari[a]; Giorgio Querzoli[a]
[a] Dipartimento di Ingegneria del Territorio, Università degli Studi di Cagliari, Cagliari, Italy

Online publication date: 22 October 2010

To cite this Article Ferrari, Simone and Querzoli, Giorgio(2010) 'Mixing and re-entrainment in a negatively buoyant jet', Journal of Hydraulic Research, 48: 5, 632 — 640
To link to this Article: DOI: 10.1080/00221686.2010.512778
URL: http://dx.doi.org/10.1080/00221686.2010.512778

Journal of Hydraulic Research Vol. 48, No. 5 (2010), pp. 632–640
doi:10.1080/00221686.2010.512778

Research paper

Mixing and re-entrainment in a negatively buoyant jet

SIMONE FERRARI *Dipartimento di Ingegneria del Territorio, Università degli Studi di Cagliari, Via Marengo, 3, 09123, Cagliari, Italy.*
Email: ferraris@unica.it

GIORGIO QUERZOLI (IAHR Member)*, Dipartimento di Ingegneria del Territorio, Università degli Studi di Cagliari, Via Marengo, 3, 09123, Cagliari, Italy.*
Email: querzoli@unica.it (author for correspondence)

ABSTRACT
An experimental study of inclined negatively buoyant jets released from a sharp-edged orifice was carried out to better understand the re-entrainment phenomenon, i.e. the mixing of jet fluid with itself instead with external fluid, and how it biases the jet behaviour. Experiments reproducing an orifice in the lateral wall of an outfall pipe on the sea bottom were conducted using light-induced fluorescence. The mean and variance of the concentration field have been determined to study the hydrodynamic features along the jet axis, including turbulent mixing and entrainment as the densimetric Froude number varies. The re-entrainment phenomenon tends to appear as the angle exceeds 75° with respect to the horizontal, and its onset occurs for lower angles as the Froude number increases. The re-entrainment biases the behaviour of the jet trajectory, making it bend on itself, and causing a reduction of both the maximum height and distance at the location where entrainment of external fluid reaches the jet axis.

Keywords: Brine discharge, inclined negatively buoyant jet, light-induced fluorescence, mixing, ocean outfall, re-entrainment

1 Introduction

A negatively buoyant jet (NBJ) corresponds to a physical phenomenon that develops if a fluid is injected upwards into a lighter or downwards into a heavier fluid. There are many practical applications involving this phenomenon, including discharges into the sea of brine from desalination plants (Cipollina *et al.* 2005, Kikkert *et al.* 2007), oil or gas-drilling facilities and mineral salt industries, e.g. from leaching of mineral salts domes (McLellan and Randall 1986), gypsum or acidic wastes from fertilizer factories (Roberts *et al.* 1997), dense effluents from wastewater treatment plants, sewerage and industrial wastes (Koh and Brooks 1975), replenishing of cold salt water at the bottom of solar ponds (Caruso *et al.* 2001), improvement of water quality by forced mixing in reservoirs, small lakes and harbours (McClimans and Eidnes 2000), forced heating or cooling of large structures such as aircraft hangars, buildings or rooms (Baines *et al.* 1990), replenishment of magma chambers in the Earth's crust (Campbell and Turner 1989) or the evolution of volcanic eruption columns (Kaminski *et al.* 2005), exit snow from snowploughs (Lindberg and Petersen 1991), vehicle exhausts from diesel engines or accidental leaks of hazardous gases (Lane-Serff *et al.* 1993).

Many studies were dedicated to vertical buoyant jets (Lin and Armfield 2000, Lawrence and Maclatchy 2001, Kuang and Lee 2001, Davidson *et al.* 2002, Lin and Linden 2005, Yannopoulos and Noutsopoulos 2006a, 2006b) and to vertical NBJs (Baines *et al.* 1990, Pantokratoras 1999, Kaminski *et al.* 2005). However, few investigations on inclined NBJs released in a stagnant environment are available. Roberts and Toms (1987) studied experimentally NBJs, released vertically or with an angle of $\theta = 60^\circ$ to the horizontal, finding that the maximum height of the 60° jet was smaller than that of the vertical jet, even if the dilution was larger in the first case. Baines *et al.* (1990) found that the maximum height for $\theta = 83^\circ$ was larger than for the vertical jet. In contrast, the investigations of Lane-Serff *et al.* (1993) for θ from 15° to 75° indicated that the final heights increase with θ. Roberts *et al.* (1997) focused on the dilution at the impact point (i.e. the point where the jet reaches again the same height of the source) and the density current that develops in 60° inclined NBJs. Cipollina *et al.* (2005) focused their laboratory investigations on the maximum height,

Revision received 27 July 2010/Open for discussion until 30 April 2011.

ISSN 0022-1686 print/ISSN 1814-2079 online
http://www.informaworld.com

distance from the source and dilution at the impact point of 30°, 45° and 60° inclined NBJs. Kikkert *et al.* (2007) carried out a similar experimental campaign with θ ranging from 5° to 75°. Bloomfield and Kerr (2002) investigated the maximum height of inclined NBJs with θ from 30° to 90°, demonstrating that the maximum height increases rapidly for small θ, in agreement with Baines *et al.* (1990), with a maximum at 80°, while the maximum height decreases for large θ. This behaviour is due to the proximity between the uprising and descending jet branches, causing re-entrainment, i.e. mixing of jet fluid with other jet fluid instead with external fluid. Despite the importance the re-entrainment process may have in practice, only a few studies mention it, focusing merely on its effect on isolated features, such as maximum jet height. Moreover, all available studies focus on the release at the end of a pipe or a nozzle. Investigations on non-buoyant jets indicate that the rate of entrainment of ambient fluid is higher in sharp-edged orifice jets than in jets issued from contoured nozzles, while jets issued from pipes provide the lowest rate (Mi *et al.* 2001, 2007). Therefore, the main purpose of this research is to detail the investigation of mixing phenomena in an NBJ released from a sharp-edged orifice, simulating the release from a standard diffuser such as an orifice in the lateral wall of an outfall pipe laid on the sea bottom, the occurrence of re-entrainment and how it biases the main jet features.

2 Relevant parameters and scales

NBJs are driven from a source of both momentum and buoyancy. Initially, momentum is dominant, so that NBJs behave basically as simple jets released with the same angle. Far from the outlet, buoyancy prevails, bending the buoyant jet, similar to a plume (Figs. 1–3). As stressed by List (1979) for a stagnant receiving fluid, the only relevant parameters characterizing the initial conditions are the initial specific flux of mass $Q = UA$, momentum $M = U^2A$ and buoyancy $B = g'UA$, where U is the mean outlet velocity, A the outlet area and $g' = g(\rho_D - \rho_R)/\rho_R$, where ρ_D is the density of discharged (subscript D) fluid, ρ_R the density of receiving (subscript R) fluid and g the gravitational acceleration. A dimensional analysis yields two independent length scales: $l_Q = Q/M^{1/2}$, representing the order of the influence length of the initial geometry on the flow, and $l_M = M^{3/4}/B^{1/2}$, representing the order of distance at which buoyancy prevails on initial momentum. These two lengths can be combined into the densimetric Froude number F as

$$\mathsf{F} = \left(\frac{\pi}{4}\right)^{1/4}\left(\frac{l_M}{l_Q}\right) = \frac{U}{(g'D)^{1/2}} \tag{1}$$

where D is the outlet diameter. All F, the Reynolds number $\mathsf{R} = UD/\nu$, where ν is the kinematic viscosity of discharged fluid, and the angle θ are the non-dimensional parameters controlling the behaviour of inclined buoyant jets. θ controls the misalignment between buoyancy and initial momentum, with the buoyant jets remaining axisymmetric only if $\theta = 90°$. In the experiments reported below, R was kept constant and high enough for the jet to be turbulent immediately beyond the vena contracta, to investigate the effects of F and θ on buoyant jets.

3 Materials and methods

The experimental set-up was designed to simulate the flow discharging from one of the lateral ports of a typical submarine outfall. Usually, these outfalls should achieve the required dilution as soon as possible via turbulent mixing by discharging through a long pipe laid on the sea bottom, terminating with diffusers, which typically include ports rising from the pipe or orifices on the pipe sides. In the present tests, the standard diffuser configuration of orifices in the lateral wall of the outfall pipe was simulated, as were widely employed in the marine outfall design since the 1960s (Rawn *et al.* 1961, Koh and Brooks 1975, Wright *et al.* 1982, Wood 1993, Avanzini 2006). A dense solution was discharged through a sharp-edged orifice outlet of diameter $D = 4.0$ mm on the wall of a cylindrical vessel of 0.10 m diameter, simulating a portion of the outfall pipe. The vessel volume was large, such that the outlet velocity profile was nearly top-hat shaped. A preliminary test series indicated that the jet remains laminar for a tract (whose length depends on R) at low R, then becomes unstable and the Kelvin–Helmholtz (KH) structures appear at its boundaries leading to the turbulent transition. Conversely, if R exceeds a critical value of ~500 in the present tests, KH instabilities begin to develop just from the orifice. Increasing R further does not change this scenario, though an effect of R can be expected, since studies on turbulent flows suggest that jets depend on R under a critical value of about 20,000 (Dimotakis 2000, Mi *et al.* 2007).

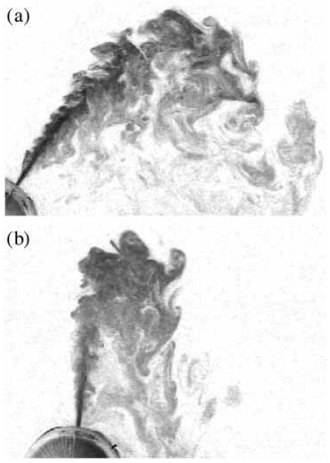

Figure 1 Two instantaneous visualizations of concentration fields for two NBJs with = 14.8: (a) $\theta = 55°$; (b) $\theta = 85°$. High concentrations are indicated by dark grey, low concentrations pale grey

A solution made up of water, sodium-sulphate (to increase the solution density) and fluorescent dye (Sodium fluorescein, for jet visualization) was released from a constant head tank into a 0.30 m wide, 21 m long flume, filled with water kept still during the tests to simulate the marine receiving body at rest. The water depth in the flume was 0.46 m, high enough to avoid an interaction between the jet and the free surface. The axial vertical jet section was illuminated from the top by a 4 mm thick light sheet, obtained with two aligned slide projectors, equipped with a black slide and a narrow, vertical slit at its centre and focused in the observational area of 0.40 m $\times$ 0.24 m. The angle of divergence of the light sheet in water was 1.56 mrad, resulting in ± 0.19 mm of the light sheet thickness along the maximum extent of the observational region. A 3-CCD video camera at the frequency of 25 Hz was used with a resolution of 720 $\times$ 576 pixels $\times$ 8 bits. This set-up provided quantitative measurements of flow density using the light-induced fluorescence (LIF) technique. The distribution of the light intensity in the observational area was measured by acquiring a reference image of the lighted background. Therefore, the intensity of the fluorescent light varied only because of the incident light. The fluorescein concentration was kept very low to avoid nonlinearity between light intensity and dye concentration and to minimize the light attenuation (Sutton *et al.* 2008). As a consequence, the salt concentration (which was directly proportional to the fractional volume of the fluorescein) was assumed proportional to the measured light intensity. Moreover, since the size of the observational area was small, the attenuation of the light intensity due to the fluorescein was found negligible. Note that the use of Sodium fluorescein as a marker for salt density is fair since the Schmidt numbers $\mathsf{S} = \nu/k$ (k indicates the molecular diffusivity) of the Sodium fluorescein ($\mathsf{S} \cong 1000$) and of the salt ($\mathsf{S} \cong 700$) have similar values. Therefore, the salt concentration is linearly related to the optically measured fluorescein concentration (Troy and Koseff 2005, Querzoli and Cenedese 2005).

In the present tests, concentrations were always evaluated after normalization by their value at the exit. Therefore, no direct calibration of LIF values against known salt concentrations was performed, and the system was un-calibrated in the sense that LIF measurements are originally obtained in arbitrary units. Different θ from 45° to 90° with a 5° step, and F from 4.9 to 40.2 were investigated, whereas the initial discharge rate and R were 3×10^{-6} $\mathrm{m^3 s^{-1}}$ and 10^3, respectively. The R used in the present tests was smaller than the threshold of 20,000 proposed for independence of the mixing processes with R (Dimotakis 2000). Therefore, when comparing the present results with high R applications, such as ocean outfalls with $\mathsf{R} \sim 10^6$ (Alameddinea and El-Fadel 2007), possible scale effect should be kept in mind. However, since it is common to perform model tests with values of R much smaller than in prototypes (e.g. Kikkert *et al.* (2007) with R from 2200 to 5400, Roberts *et al.* (1997) with R from 2800 to 4400, Cipollina *et al.* (2005) from 2500 to 10,400, or Shao and Law (2006) from 1390 to 4456), scale effects have been discussed. Tian *et al.* (2004) argued that, in contrast with flows interacting with solid boundaries, free-shear flows such as jets and plumes do not strongly depend on R; Koh *et al.* (1983) suggested that a low R, possibly generating an initially laminar jet, may cause a reduced entrainment in the initial stage of the buoyant-jet and, conservatively, a slightly lower final dilution; Roberts *et al.* (1989) performed tests to quantify scale effects for $\mathsf{R} = 546$, 1073 and 1481, yet found none. Density differences, ranging from 59 $\mathrm{kg{\cdot}m^{-3}}$ to 0.9 $\mathrm{kg{\cdot}m^{-3}}$, were measured by means of a buoyancy-type densitometer. Two visualizations of instantaneous flow fields are shown in Fig. 1. The concentration field was obtained from digitized RGB image sequences by analysing their green component. First, a reference, background image was obtained by recording just before a test, 100 images without jet and computing their average. Secondly, the background was subtracted from each image, and the resulting field was normalized by the grey level measured at the outlet, corresponding to the initial concentration. Under the hypothesis of ergodicity, the statistics of the concentration field were obtained by time averaging, performed over 5000 samples for each run. The jet axis, assumed to coincide with the locus of the concentration maxima on jet cross-sections, was determined by an iterative procedure. In the first iteration, the area above two straight lines, L1 and L2, was identified (Fig. 2, with X and Y being horizontal and vertical coordinates, measured from the outlet). Point P was taken arbitrarily in the region beneath the jet; then, L1 was determined as the straight line passing through P and the jet origin (black asterisk in Fig. 2) and L2 as the horizontal straight line through P. The first approximation axis (white line in Fig. 2) was computed as the locus of concentration maxima (circles in Fig. 2) on a pencil of half-lines originating from P and ranging from L1 and the horizontal line L2 (dotted lines in Fig. 2). In the successive iterations, series of sections, orthogonal to the current axis guess, were used to find new concentration maxima and the next axis guess. Usually three iterations were sufficient for convergence of the procedure.

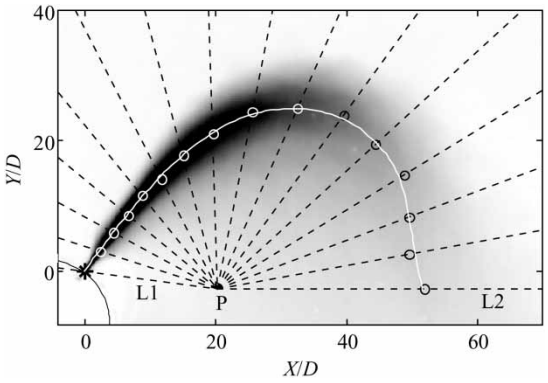

Figure 2 Sketch of computation of first iteration jet axis over non-dimensional mean concentration field for jet of Fig. 1(a). X and Y are horizontal and vertical coordinates, with origin at outlet, non-dimensionalized by outlet diameter D

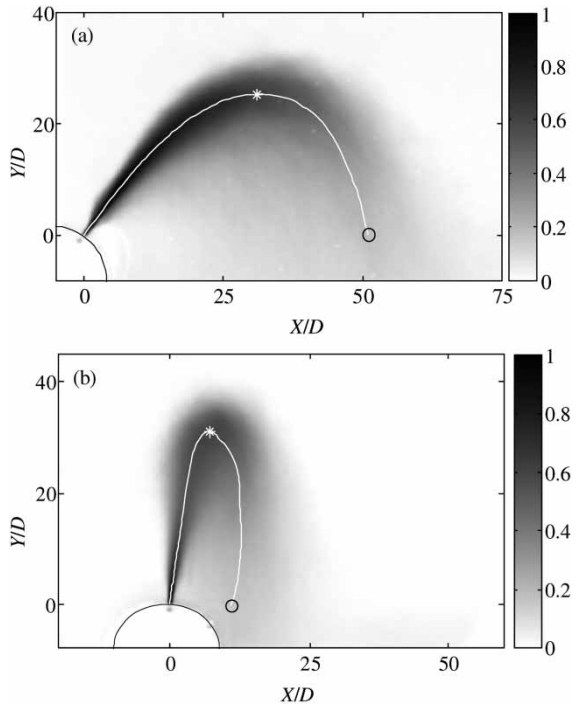

Figure 3 Non-dimensional mean concentration fields for jets of Fig. 1 with (white line) jet axis, (white asterisk) point of maximum height and (○) impact point

The jet axis, computed following the above procedure, is shown as a white line in Fig. 3 and as a black line in Fig. 4.

4 Discussion

4.1 *General behaviour of NBJs*

Figure 1 shows that NBJs released from a sharp-edged orifice cover an initial distance conserving more or less their initial diameter D. Subsequently, the onset of KH instability causes a sudden widening, as the billows grow and drag external fluid into the jet, increasing mixing and dilution. After the initial stage of fast growth, the KH waves break, with an intense production of turbulence and mixing, which propagate through the whole jet width, so that patches of ambient fluid reach the jet centre. Except for the initial stage, the growth-rate is remarkably asymmetrical since the stable stratification at the upper jet boundary is opposed to mixing and entrainment, whereas the unstable stratification at the lower border tends to enhance jet widening (Querzoli and Cenedese 2005). Accordingly, Fig. 1 shows that, at the upper border, local stability permits the complete development of compact KH billows before their breaking, whereas the local unstable stratification tends to transform the growing waves in plumes propagating downwards at the lower boundary.

The above-described behaviour is observed also in Figs. 3 and 4, showing the mean and the variance of non-dimensional concentration C/C_{MAX}, where C is the concentration and C_{MAX} the outlet concentration, for the conditions of Fig. 1. The variance of the concentration is non-dimensionalized by the square of the maximum concentration. The mean field is symmetrical in the first part, where the flow is driven essentially by initial momentum. Then, as the buoyancy becomes relevant, the span-wise sections become neither symmetrical nor self-similar. Above the axis, there is a narrow region characterized by high upward concentration gradients, below there is a wide region of smooth variation of the concentration. The variance is a minimum in the central jet region, increasing toward the upper and lower boundaries (Fig. 4). As consequence of the stable stratification at the upper boundary, the maximum values of the variance are located in the upper, external region, where KH waves develop upwards but rapidly break, because of downwards buoyancy contrasting their growth. This causes, at a fixed point, sudden changes in the light intensity and thereby a high variance.

In contrast, as a consequence of unstable stratification at the lower boundary, the downward-developing, plume-like structures are driven away from the jet by buoyancy, leading to more distributed but less intense concentration fluctuations. The variance remains low in the central jet portion for a longer distance, until it is also reached by the intense perturbations generated at the shear-layer. At that stage, the entraining, external fluid has reached the whole jet.

Figures 3(b) and 4(b) show that, for high $\theta = 85^\circ$, the uprising and descending jet portions tend to interact; so the lower boundary is not a zone of entrainment of external fluid, but only a region of mixing between the ascending and descending

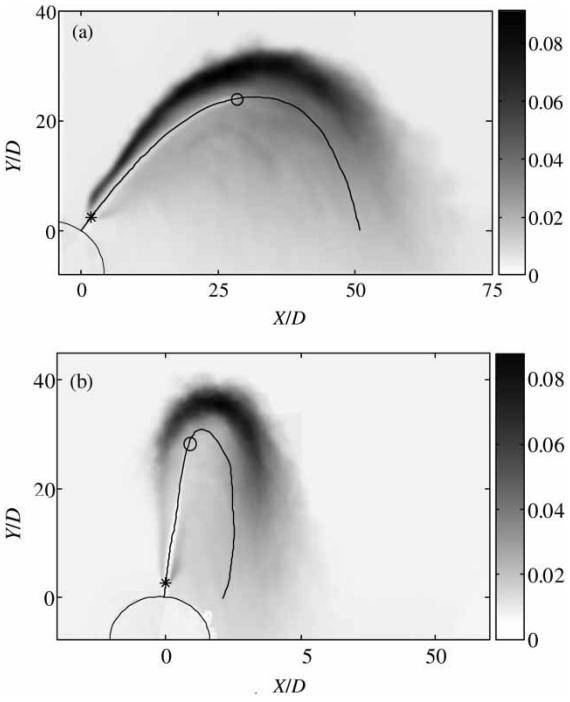

Figure 4 Maps of variance of concentration, non-dimensionalized by square of maximum concentration, for jets of Fig. 1, with (—) jet axis, (*) point of onset of KH instability and (○) point where entrainment reaches jet axis

jet fluid, namely re-entrainment. The evidence of this interaction is given in Fig. 5, where the mean concentration field for $\theta = 85^\circ$, and three cross-sectional profiles are plotted. The first profile was taken along the upflow at $s/D = 24$; the remaining two are taken on the downflow at $s/D = 86$ and $s/D = 105$. Here, s is the downstream distance measured along jet axis. The profiles are characterized by two main peaks: one sharp, corresponding to the uprising branch, and one broader at the intersection with the descending branch. One peak is always centred on the origin (as the span-wise abscissa r is measured from the axis), whereas the other corresponds to the opposite branch. There is no region of separation, with negligible concentration, in between but the two branches are contiguous thus exchanging mass, tracer and momentum. As shown below, the fluxes among these branches affect the jet behaviour. The mass exchange modifies its trajectory, the tracer exchange tends to reduce the dilution and the exchange of momentum enhances the velocity decrease along its axis, thus shortening its path.

4.2 *Jet axis*

Figure 6 shows the jet axes for $\theta = 50^\circ$ and $\theta = 85^\circ$, and F ranging from 8 to 30. As F decreases, the curvature of the jet axis increases and the length of the path decreases. For $\theta = 50^\circ$, the axes exhibit a parabolic-like shape with upward and downward arc braches which are nearly symmetrical, except

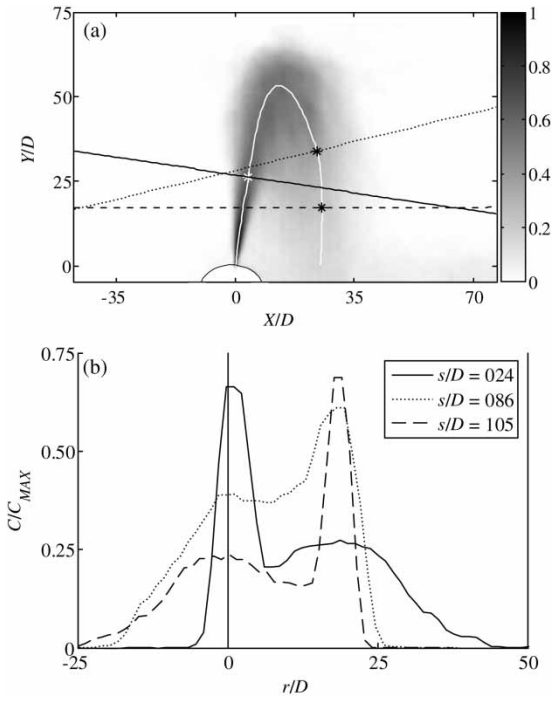

Figure 5 Jet with re-entrainment for $\theta = 85^\circ$, F = 30.8: (a) non-dimensional mean concentration C/C_{MAX} field and jet axis, (b) three cross-sectional concentration profiles, measured at downstream distance along jet axis $s/D = 24$ (—, upward branch), $s/D = 86$ (···, downward branch) and $s/D = 105$ (- - -, downward branch), (*) origin of span-wise abscissa r/D

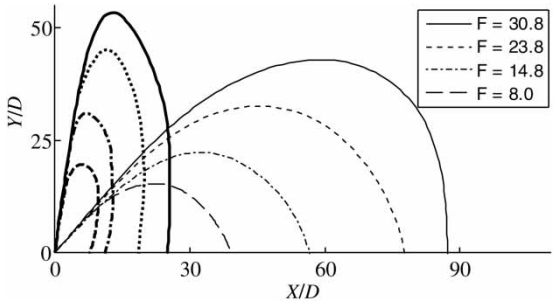

Figure 6 Jet axis for jets of constant θ (− − 50°, — — 85°) and variable F

for F = 30, where buoyancy prevails in the last part of the path and the descending branch is steeper than the ascending. This is in agreement with Cipollina *et al.* (2005) for large F (where it is stressed that the jet falls down rapidly after reaching its maximum, due to the effect of negatively buoyancy flux) and shows how NBJs tend to change the behaviour as F increases. Conversely, the trajectories for $\theta = 85^\circ$ are non-symmetrical and far from being parabola-like since the descending branch tends to bend towards the ascending, due to re-entrainment. In the region of interaction, the mass flux due to the mutual entrainment among the ascending and descending branches causes a Coanda effect. In the initial portion, the jet is mainly driven by initial momentum, with a small effect of re-entrainment yet the effect of re-entrainment becomes significant and the curvature of the axis enhanced as distance increases, bending the jet on itself, especially in the descending branch. This phenomenon was observed in all the cases, but it is more pronounced as F decreases. The effect of θ on re-entrainment is shown in Fig. 7, where the jet axes at F = 23.8 and θ from 45° to 90° are plotted. As θ increases, the impact point, i.e. the point where the axis intercepts again the horizontal line at $Y/D = 0$, approaches the origin, while the maximum height increases for θ from 45° to 80°. Increasing further θ, the ascending and descending jet branches begin to interact, causing re-entrainment. The axes tend to bend on themselves and the effect of mutual momentum flux prevents the jets to raise more. As a consequence, the maximum height decreases for 85° and 90°. This is in agreement with Bloomfield and Kerr (2002), who observed that the maximum height is reached at $\theta \cong 80^\circ$.

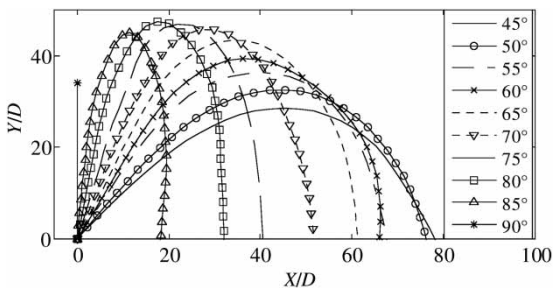

Figure 7 Jet axis for F = 23.8 and variable θ

4.3 *Characteristic dimensions of jet axis*

The impact distance (subscript d) x_d and the maximum height (subscript h) y_h were identified as characteristic features of the jet axis, with x_d the horizontal distance between outlet and impact point, and y_h the vertical distance between outlet and the highest point reached by the axis. In Fig. 8(a), x_d was non-dimensionalized by ($D\mathsf{F}$) and plotted versus θ. Following List (1979), who pointed at the importance of the horizontal momentum component in determining x_d, the experimental data were approximated as

$$\frac{x_d}{(D\mathsf{F})} = a(\cos\theta)^{3/4} \tag{2}$$

Although this does not account for the complexity of the phenomenon, the resulting curve seems to fit well the test data, with $a = 5.29 \pm 1.22$. The agreement is good also for the angles where re-entrainment appears, because the displacement of the impact point due to axis bending is small with $x_d = 0$ for $\theta = 90^\circ$. List's (1979) dimensional considerations suggest $y_h \sim (\sin\theta)^{3/4}$. However, the test results reported here and by Bloomfield and Kerr (2002) do not fit such a curve (Fig. 8b). Rather, the test data seem to arrange along straight lines passing through the origin (as expected, y_h equals 0 in NBJs released horizontally), according to

$$\frac{y_h}{(D\mathsf{F})} = b\theta \tag{3}$$

with $b = 1.79 \pm 0.32$. Comparing the empirical linear fit with the $(\sin\theta)^{3/4}$ fit, the test data are seen to decrease more steeply with decreasing angles than predictions based on dimensional analysis. This suggests that for small θ, the behaviour of y_h is not only biased by the vertical momentum component but the interaction with the bottom surface plays a prominent role in addition. The effect of re-entrainment is demonstrated by the deviation from the linear trend at higher θ, which is anticipated for the jets with the largest F. For $\mathsf{F} = 30.8$, the deviation appears as $\theta > 70^\circ$, whereas for $\mathsf{F} = 8$ the measured y_h are close to the linear interpolation up to 80°. Moreover, for F larger than investigated herein, re-entrainment will tend to appear for smaller θ as F controls the trajectory. In Fig. 8, y_h and x_d of the present study are also compared with test data of Cipollina *et al.* (2005) for $\theta = 45^\circ$ and 60°, $\mathsf{F} \geq 14$ (among the 45 runs, only two include $\mathsf{F} < 18$), Roberts *et al.* (1997) for $\theta = 60^\circ$, $\mathsf{F} \geq 18.7$, Shao and Law (2006) for $\theta = 30^\circ$ and 45°, $\mathsf{F} \geq 10$ (among 10 runs, only two include $\mathsf{F} < 15$), Zeitoun *et al.* (1972) and with the analytical solution of Kikkert *et al.* (2007) for both pipes or nozzles. The analytical solution of Kikkert *et al.* (2007) was validated with test including $\theta = 45^\circ$–75° and $\mathsf{F} \geq 27$. They indicated for $\theta \geq 75^\circ$ that re-entrainment begins to show its effects and the analytical solution is no longer valid. In spite of the different initial conditions and R (see Section 3), y_h is in good agreement over the entire range of F used to validate the formulas.

Differences especially in x_d are observed only for $\mathsf{F} < 14.8$, substantially out of the range of the test data used to calibrate the above formulas. At the smallest F, no literature test data are available, but the present data indicate larger y_h and x_d than predicted. This behaviour is in agreement with Roberts and Toms (1987), indicating that $y_h/(D\mathsf{F})$ depends on F for small F. The semi-empirical Eq. (2) tends to overestimate x_d, in particular for low θ, due to the data with a small F. Differently, Eq. (3) fits the data better, and seems to be a good linear approximation of the solution by Kikkert *et al.* (2007). A slight overestimation is due to the data points at $\mathsf{F} = 8.0$, whereas those from $\mathsf{F} = 14.8$ collapse quite well with the general trend. Note that the definition of jet axis used herein is different from that of Kikkert *et al.* (2007). Herein the jet axis is defined as the locus of the concentration maxima, whereas Kikkert *et al.* (2007), following Davidson and Pun (2000), define the jet axis as the locus of the mass centre of the spanwise jet sections. Due to buoyant-jet asymmetry, this centreline is a line which is always closer to the centre of curvature than the axis from the present data. The difference between these definitions is more significant as the spanwise concentration distribution becomes more skewed, i.e. for low F, and partially explains the difference in x_d and y_h for the smallest F.

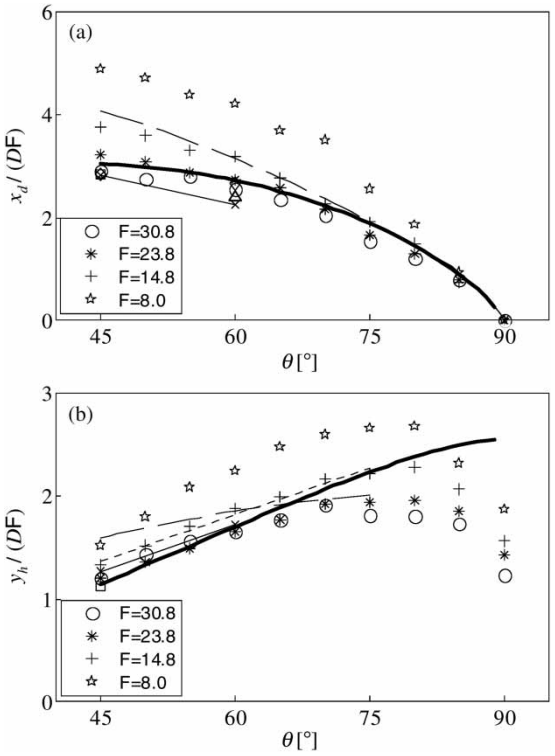

Figure 8 Comparison of (a) non-dimensional impact distance $x_d/(D\mathsf{F})$ and (b) non-dimensional maximum jet height $y_h/(D\mathsf{F})$, measured in the present study for various F with data of (x—x) Cipollina *et al.* (2005), (Δ) Roberts *et al.* (1997), (□) Shao and Law (2006), (◇) Zeitoun *et al.* (1972), (—) analytical solution by Kikkert *et al.* (2007), best fit with (– – in a) Eq. (2), (– – in b) $y_h \sim \sin^{3/4}$, and (···) Eq. (3)

4.4 *Distances of instability onset and of jet axis entrainment*

The onset of the KH instability plays a fundamental role in the entrainment mechanism because the billows, during their initial development, drag external fluid into themselves and then break, causing mixing, thereby initiating entrainment in the external jet region where KH instability takes place. As the onset of this instability causes high concentration fluctuations, this phenomenon was investigated via concentration variance. The distance d_{KH} of KH (subscript KH) instability onset, i.e. the axial distance between the point of initial development of the KH instability (Fig. 4) and jet origin, was plotted versus F for the various θ (Fig. 9). Note that buoyancy destabilizes the jet because the instability develops prior to lower F, i.e. for higher buoyancy, while the data referring to the same F almost collapse, evidencing that d_{KH} is independent from θ. To highlight the direct dependence of d_{KH} on F, the data of Fig. 9 were approximated with a straight line as

$$\frac{d_{\mathrm{KH}}}{D} = 0.08 \cdot \mathsf{F} + 1.31. \tag{4}$$

While the external jet portion exhibits intense fluctuations at a small distance from the origin because of the onset of the KH instability, the inner portion remains relatively undisturbed over a longer distance, until the perturbations generated at the boundary propagate to the jet centre, and the entrained ambient fluid spreads over the entire jet width. The entrainment of external fluid at the jet axis is shown in Fig. 10, where non-dimensional concentration variance along the axis $\sigma^2/C^2{}_{MAX}$ is plotted for the jets shown in Fig. 1. The variance slightly increases in the initial portion, where the released fluid of quite uniform concentration mixes mainly with itself. Then, a sudden change in the slope of the curve indicates that, as the perturbations generated by the large-scale structures (originating at the shear layer) propagate to the jet centre, patches of external fluid reach the axis, causing high fluctuations of concentration. This point is highlighted in Figs. 4 and 10. Note that the drop in $\sigma^2/C^2{}_{MAX}$ beyond its maximum is due to the decrease in the mean concentration caused by the dilution and due to the progressive mixing, which tends to reduce the concentration fluctuations in the jet centre. The presence of a region of low variance, which gradually narrows during jet development, is shown also in Fig. 11, where spanwise profiles of non-dimensional variance of the concentration are plotted for $\mathsf{F} = 14.8$ and $\theta = 55^\circ$. The low variance region vanishes as it is reached by zones of higher variance propagating inward from the external jet regions.

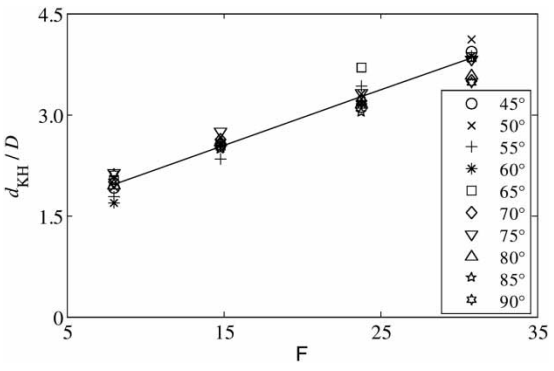

Figure 9 Non-dimensional distance of KH instability onset d_{KH}/D versus F for various θ, with (—) Eq. (4)

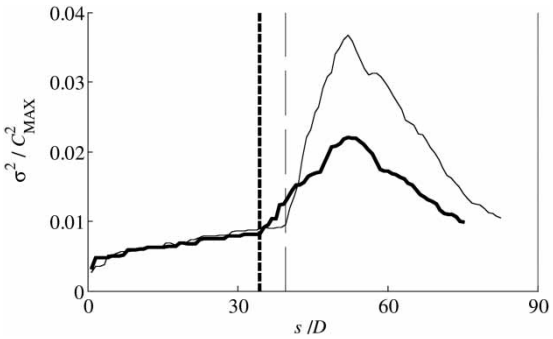

Figure 10 Variance of non-dimensional concentration $\sigma^2/C^2{}_{MAX}$ along jet axis for jets of Fig. 1 (—50°, – 85°)

This means that the slope change observed in Fig. 10 is caused by turbulence generated in the region of stable stratification. Note that d_e – the distance between origin and point where the entrainment (subscript e) reaches the jet axis (causing the sudden slope increase in Fig. 10) – is plotted versus F for various θ in Fig. 12. Similar to what was found for d_{KH}, d_e is shorter for lower F, confirming that buoyancy tends to enhance mixing, in agreement with Querzoli and Cenedese (2005) and Russ and Strykowski (1993). To highlight the effect of re-entrainment on the NBJs released upward with $\theta > 80^\circ$, the relationship $d_e(\mathsf{F})$ was fitted as straight lines for all data θ from 45° to 80°, for $\theta = 85^\circ$, and for $\theta = 90^\circ$ as

$$\frac{d_e}{D} = 2.45 \cdot \mathsf{F} + 6.75 \qquad \text{for} \quad 45^\circ \le \theta \le 80^\circ \tag{5}$$

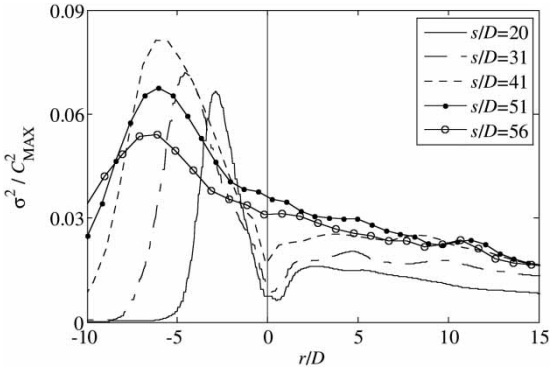

Figure 11 Spanwise profiles of non-dimensional concentration variance $\sigma^2/C^2{}_{MAX}$ for $\mathsf{F} = 14.8$ and $\theta = 55^\circ$; s/D = downstream distance measured along jet axis

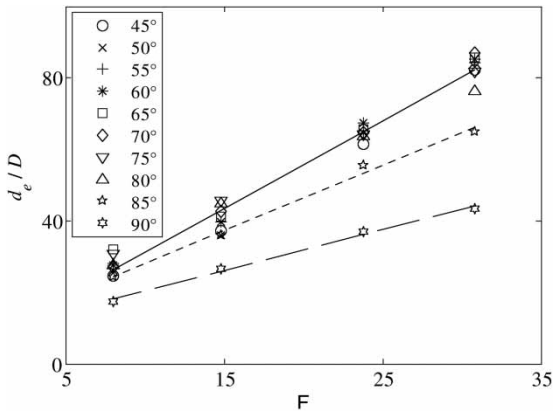

Figure 12 Non-dimensional distance $d_e/D(\mathsf{F})$ with (—) Eq. (5), (···) Eq. (6) and (- - -) Eq. (7)

$$\frac{d_e}{D} = 1.83 \cdot \mathrm{F} + 9.77 \qquad \text{for } \theta = 85^{\mathrm{o}}, \text{ and} \tag{6}$$

$$\frac{d_e}{D} = 1.13 \cdot \mathrm{F} + 9.16 \qquad \text{for } \theta = 90^{\mathrm{o}} \tag{7}$$

The good agreement with these curves suggests that there is a direct proportionality between d_e and F, in agreement with Querzoli and Cenedese (2005). Differently from d_{KH}, d_e seems to be independent of θ only for $\theta \leq 80^\circ$. Beyond this value, the coefficient of proportionality is smaller, as shown by the reduced inclination of the straight lines for 85° and 90°. This is due to the additional perturbation caused by the interaction between the ascending and the descending jet portions, because angles of 85° and 90° generate re-entrainment. Moreover, the trend of these lines suggests an increase in the re-entrainment effect with F, as the distance from the lines relative to 85° and 90° and that relative to other angles increases with F. In conclusion, effects of re-entrainment on d_e result for $\theta > 80^\circ$ but, as was stated for the maximum height, re-entrainment will tend to appear for smaller θ and large F.

5 Conclusions

The effect of re-entrainment phenomena on the characteristic parameters of inclined NBJs released from a sharp-edged orifice has been investigated via image analysis techniques. The mean concentration fields were used to identify the jet axis and to study its characteristic dimensions. The impact distance and the maximum jet height are demonstrated to depend linearly on the horizontal momentum component without any explicit dependence on re-entrainment. The maximum jet height does not only depend on the vertical momentum component, as re-entrainment for jet angles larger than 80° has an important role, causing its reduction. Moreover, re-entrainment makes the jet axis bent on itself.

The variance of the concentration fields was used to study two parameters influencing mixing, namely the distance of the KH instability onset and the distance where the entrainment reaches the jet axis. The former is directly proportional to the densimetric Froude number and independent from both the jet angle and re-entrainment; the latter directly depends on the densimetric Froude number but is independent of the jet angle only below 80°. Above this value, re-entrainment arises, causing additional mixing due to the interaction between the ascending and the descending jet branches, and reduces the entrainment distance. Angles of 85° and 90° are indeed those for which re-entrainment was observed. Re-entrainment therefore arises on inclined NBJs released from a sharp-edged orifice for jet angles larger than around 80°.

Notation

A = outlet area (m^2)
B = initial specific buoyancy flux of (m^4s^{-3})
D = outlet diameter (m)
d_e = distance of entrainment at jet axis (m)
d_{KH} = distance of KH instability onset (m)
F = densimetric Froude number (–)
g = gravitational acceleration (ms^{-2})
g' = effective gravitational acceleration (ms^{-2})
k = molecular diffusivity (m^2s)
l_M = buoyancy length scale (m)
l_Q = kinematic length scale (m)
M = initial specific momentum flux of (m^4s^{-2})
Q = initial volume flux (m^3s^{-1})
R = Reynolds number (–)
S = Schmidt number (–)
U = mean outlet velocity (ms^{-1})
x_d = impact distance (m)
y_h = maximum jet height (m)
θ = release angle from horizontal (°)
ν = kinematic viscosity of discharged fluid (m^2s)
ρ_D = density of discharged fluid (kgm^{-3})
ρ_R = density of receiving fluid (kgm^{-3})

References

Alameddinea, I., El-Fadel, M. (2007). Brine discharge from desalination plants: A modeling approach to an optimized outfall design. *Desal.* 214(1–3), 241–260.

Avanzini, C. (2006). An outline of common practical problems and solutions in the diffusers design. Proc. 4th Intl. Conf. *Marine Waste Water Disposal and Marine Environment* & 2nd Intl. Exhibition *Materials, Equipment and Services for Coastal Waste Water Treatment Plants, Outfalls and Sealines* Antalya, Turkey, Mem Ajans, Istanbul [DVD].

Baines, W.D., Turner, J.S., Campbell, I.H. (1990). Turbulent fountains in an open chamber. *J. Fluid Mech.* 212, 557–592.

Bloomfield, L.J., Kerr, R.C. (2002). Inclined turbulent fountain. *J. Fluid Mech*. 451, 283–294.

Campbell, I.H., Turner, J.S. (1989). Fountains in magma chambers. *J. Petrol.* 30, 885–923.

Caruso, G., Naviglio, A., Principi, P., Ruffini, E. (2001). High-energy efficiency desalination project using a full titanium desalination unit and a solar pond as the heat supply. *Desal.* 136, 199–212.

Cipollina, A., Brucato, A., Grisafi, F., Nicosia, S. (2005). Bench scale investigation of inclined dense jets. *J. Hydraulic Eng*. 131(11), 1017–1022.

Davidson, M.J., Pun, K.L. (2000). Locating discharge trajectories in still and moving ambient fluids. *J. Hydraulic Eng*. 126(7), 513–524.

Davidson, M.J., Gaskin, S., Wood, I.R. (2002). A study of a buoyant axisymmetric jet in a small co-flow. *J. Hydraulic Res*. 40(4), 477–489.

Dimotakis, P. (2000). The mixing transition in turbulent flows. *J. Fluid Mech*. 409, 69–98.

Kaminski, E., Tait, S., Carazzo, G. (2005). Turbulent entrainment in jets with arbitrary buoyancy. *J. Fluid Mech*. 526, 361–376.

Kikkert, G.A., Davidson, M.J., Nokes, R.I. (2007). Inclined negatively buoyant discharges. *J. Hydraulic Eng*. 133(5), 545–554.

Koh, R.C.Y., Brooks, N.H. (1975). Fluid mechanics of wastewater disposal in the ocean. *Ann. Rev. Fluid Mech*. 7, 187–211.

Koh, R.C.Y., Isaacson, M.S., Brooks, N.H. (1983). Plume dilution for diffusers with multiport risers. *J. Hydraulic Eng*. 109(2), 199–220.

Kuang, C.P., Lee, J.H.W. (2001). Effect of downstream control on stability and mixing of a vertical plane buoyant jet in confined depth. *J. Hydraulic Res*. 39(4), 375–391.

Lane-Serff, G.F., Linden, P.F., Hillel, M. (1993). Forced angled plumes. *J. Hazardous Mat*. 33, 75–99.

Lawrence, G.A., Maclatchy, M.R. (2001). Radially spreading buoyant flows. *J. Hydraulic Res*. 39(6), 583–590.

Lin, W., Armfield, S.W. (2000). Direct simulation of weak axisymmetric fountains in a homogeneous fluid. *J. Fluid Mech*. 403, 67–88.

Lin, Y.J.P., Linden, P.F. (2005). The entrainment due to a turbulent fountain at a density interface. *J. Fluid Mech*. 542, 25–52.

Lindberg, W.R., Petersen, J.D. (1991). Negatively buoyant jet (or plume) with application to snowplow exit flow behaviour. *Transportation Res. Record*. 1304, 219–229.

List, E.J. (1979). Turbulent jets and plumes. *Mixing in inland and coastal water*, 315–389, H.B. Fisher, E.J. List, R.C.Y. Koh, J. Imberger, N.H. Brooks, eds. Academic Press, New York.

McClimans, T., Eidnes, G. (2000). Forcing nutrients to the upper layer of a fjord by a buoyant plume. Proc. 5th Intl. Symp. *Stratified Flows*, Vancouver, 199–204.

McLellan, T.N., Randall, R. (1986). Measurement of brine jet height and dilution. *J. Waterw., Port, Coast, Ocean Eng.* 112(2), 200–216.

Mi, J., Kalt, P., Nathan, G.J., Wong, C.Y. (2007). PIV measurements of a turbulent jet issuing from round sharp-edged plate. *Exp. Fluids* 42(4), 625–637.

Mi, J., Nathan, G.J., Nobes, D.S. (2001). Mixing characteristics of axisymmetric free jets from a contoured nozzle, an orifice plate and a pipe. *J. Fluid Eng.* ASME 123(4), 878–883.

Pantokratoras, A. (1999). Vertical penetration of inclined heated water jets discharged downwards. *J. Env. Eng*. 125(4), 389–393.

Querzoli, G., Cenedese, A. (2005). On the structure of a laminar buoyant jet released horizontally. *J. Hydraulic Res*. 43(1), 71–85.

Rawn, A.M., Bowerman, F.R., Brooks, N.H. (1961). Diffusers for disposal of sewage in sea water. *Trans. ASCE* 126, 344–388.

Roberts, P.J.W., Toms, G. (1987). Inclined dense jets in flowing current. *J. Hydraulic Eng*. 113(3), 323–341.

Roberts, P.J.W., Ferrier, A., Daviero, G. (1997). Mixing in inclined dense jets. *J. Hydraulic Eng*. 123(8), 693–699.

Roberts, P.J., Snyder, W.H., Baumgartner, D.J. (1989). Ocean outfalls 1: Submerged wastefield formation. *J. Hydraulic Eng*. 115(1), 1–25.

Russ, S., Strykowski, P.J. (1993). Turbulent structure and entrainment in heated jets: The effect of initial conditions. *Phys. Fluids* A 5(12), 3216–3225.

Shao, D., Law, A.W.K. (2006). Desalination discharges in shallow coastal waters. Proc. 4th Intl. Conf. *Marine Waste Water Disposal and Marine Environment* & 2nd Intl. Exhibition *Materials, Equipment and Services for Coastal Waste Water Treatment Plants, Outfalls and Sealines* Antalya, Turkey, Mem Ajans, Istanbul [DVD].

Sutton, J.A., Fisher, B.T., Fleming, J.W. (2008). A laser-induced fluorescence measurement for aqueous fluid flows with improved temperature sensitivity. *Exp. Fluids* 45(5), 869–881.

Tian, X., Roberts, P.J.W., Daviero, G.J. (2004). Marine wastewater discharges from multiport diffusers 1: Unstratified stationary water. *J. Hydraulic Eng*. 130(12), 1137–1146.

Troy, C.D., Koseff, J.R. (2005). The generation and quantitative visualization of internal breaking waves. *Exp. Fluids* 38(5), 549–562.

Wood, I.R. (1993). The dilution from a standard diffuser. *Ocean disposal of wastewater*, 71–84, I.R. Wood, R.G. Bell, D.L. Wilkinson, eds. World Sci. Publ., Singapore.

Wright, S.J., Wong, D.R., Zimmerman, K.E., Wallace, R.B. (1982). Outfall diffuser behaviour in stratified ambient fluid. *J. Hydraulics Div.* ASCE 108(HY4), 483–501.

Yannopoulos, P.C., Noutsopoulos, G.C. (2006a). Interaction of vertical round turbulent buoyant jets 1: Entrainment restriction approach. *J. Hydraulic Res*. 44(2), 218–232.

Yannopoulos, P.C., Noutsopoulos, G.C. (2006b). Interaction of vertical round turbulent buoyant jets 2: Superposition method. *J. Hydraulic Res*. 44(2), 233–248.

Zeitoun, M.A., Reid, R.O., McHilhenny, W.F., Mitchell, T.M. (1972). Model studies of outfall systems for desalination plants. *Res. and Devel. Progress Rep.* 804. Office of Saline Water, U.S. Dept. of the Interior, Washington DC.